Rare Metal Materials and Engineering
Volume 52, Issue 2, February 2023
Available online at www.rmme.ac.cn

Science Press

Cite this article as: Guo Yinchen, Yang Jiancan, Zhou Shaoxin, et al. Microstructure and Properties of Nanometer- and Micrometer-Sized Rare-Earth Oxide Doped W-La_2O_3-Y_2O_3-ZrO_2 Cathode Tip[J]. Rare Metal Materials and Engineering, 2023, 52(02): 416-425.

ARTICLE

Microstructure and Properties of Nanometer- and Micrometer-Sized Rare-Earth Oxide Doped W-La_2O_3-Y_2O_3-ZrO_2 Cathode Tip

Guo Yinchen[1], **Yang Jiancan**[1], **Zhou Shaoxin**[1], **Yuan Delin**[2], **Nie Zuoren**[1]

[1] College of Materials Science and Engineering, Beijing University of Technology, Beijing 100124, China; [2] Jiangxi College of Applied Technology, Ganzhou 341000, China

Abstract: Nanometer-(70–80 nm) and micrometer-sized (500–600 nm) rare-earth (RE) oxides (La_2O_3, Y_20_3) were separately mixed with tungsten powder by a mechanical alloying method. Afterwards, the W-1.5La_2O_3-0.1Y_2O_3-0.1ZrO_2 (wt%) was prepared by cold isostatic pressing, medium-frequency induction sintering, rotary forging, and drawing. Then we performed tungsten argon arc welding (TIG) under the same welding current for 0.5, 1, and 2 h on the cathode samples containing, separately, nanometer- and micrometer-sized RE oxides. Results show that the sample with nanometer-sized RE oxides exhibits higher working stability during the welding process, and the burning loss is decreased by nearly 85.4%. Moreover, with prolonging the working time, the aggregation degree of RE oxides in different regions of the tip significantly increases. Combined with the temperature simulation by COMSOL Multiphysics, we found that the diffusion activation energy of the second phase is decreased by nearly 34%. This is because the finer second phase effectively controls the evolution of the tungsten matrix structure, thus preserving many grain boundaries as channels and promoting the diffusion of active substances.

Key words: W-La_2O_3-Y_2O_3-ZrO_2; tungsten cathode; TIG; rare-earth oxides; nanometer-sized; micrometer-sized; COMSOL Multiphysics

Tungsten cathodes are one of the key heat source materials widely used in argon arc welding, plasma welding, spraying, cutting technology, and metallurgical industry[1–3]. As electron and ion sources, tungsten cathodes function on the principle of the thermal emission of electrons from the working surface, and they belong to thermionic emission materials. Originally, pure tungsten cathodes were widely used in this field, precisely featuring high melting point and low vapor pressure. It was later found that adding some alloying elements can significantly reduce the electron work function and improve the working performance of tungsten cathodes. Among alloying elements, rare-earth (RE) oxides have a small electron work function. During the activation of tungsten cathodes, RE can migrate and diffuse from the body to the surface of cathode, forming an active layer, thereby promoting emission and improving electron emission performance. Numerous studies[4–16] reported that adding various RE elements in the form of oxides can optimize the performance of the pure tungsten cathode. The structure of thermionic emission materials becomes a basic research hotspot, especially in the development of nanomaterials science, and the research yields successful development of nanocomposite oxides-tungsten thermionic emission materials[17–21]. The application on single RE tungsten cathodes has matured, and the industrial production is now implemented. However, due to its poor welding stability and other properties, single RE tungsten cathode can only be used under specific working conditions and cannot fully replace pure tungsten cathodes[22–24]. Currently, thermionic emission materials made from compounding various RE oxides and tungsten represent a promising development direction. Combined with Ref. [25–26] and the results of a long-term research by our research

---

Received date: September 01, 2022
Foundation item: National Natural Science Foundation for Innovative Research Groups Projects (51621003)

Corresponding author: Yang Jiancan, Ph. D., Professor, College of Materials Science and Engineering, Beijing University of Technology, Beijing 100124, P. R. China, E-mail: yjcan@bjut.edu.cn

group, it is established that a multi-component composite W-La_2O_3-Y_2O_3-ZrO_2 tungsten cathode exhibits the best comprehensive performance.

At high temperatures, the used cathode undergoes fast evaporation of the active RE material on the surface. If the RE elements inside the cathode cannot diffuse and migrate to the working surface in a given time, the working stability of cathode is greatlyed affected. Thus, it is necessary to control the growth rate of tungsten grains at high temperatures so that more grain boundaries can be preserved as diffusion channels to improve the diffusion mobility of RE. The finely dispersed second phase can hinder the grain growth of the matrix during high-temperature processing, so the average size of tungsten grains can be significantly reduced[27–32].

In the present study, we used powder metallurgy to separately add nanometer- and micrometer-sized RE oxides as the second phase to synthesize W-La_2O_3-Y_2O_3-ZrO_2 with fine and dispersed second-phase particles in the finished cathode. The tungsten argon arc welding (TIG) was performed on the two kinds of prepared cathodes doped with different particle sizes of RE oxides, and the effect of adding RE oxides with different particle sizes on the microstructure and working performance was discussed.

1 Experiment

The purity of tungsten powder (Ganzhou Hongfei Tungsten and Molybdenum Company) with the average particle size 1.5 μm and nanometer- and micrometer-sized RE oxides powders (Xuzhou Boguan Welding Company) was 99.9%. Two composite powders were prepared, and the average particle size of micrometer-sized RE oxides and nanometer-sized RE oxides was 500 – 600 nm and 70 – 80 nm. ZrO_2 (Beijing Jia Shi Teng Trading Company) had a purity of 99% and an average particle size of 20 μm.

The tungsten powder, RE oxides, and zirconium hydride were used as raw materials to prepare W-1.5La_2O_3-0.1Y_2O_3-0.1ZrO_2 (wt%). After ball milling and ultrasonic mixing, the composite powders, with micrometer-sized (W-1) and nanometer-sized (W-2) RE oxides, exhibit irregular polyhedral morphology, as shown in Fig. 1. The steps of ultrasonic powder mixing is as follows: put the powder into a beaker and add an appropriate amount of alcohol; then, put the beaker into an ultrasonic cleaner to work for 10 min, and then take it out and put in a vacuum drying oven. In this experiment, the bulk density, tap density, and Fisher particle size of the powder were characterized and analyzed. The basic test method of Fisher Sub-Sive Sizer (Fsss) was a steady-flow air permeation method, i. e. the specific surface area and average particle size were determined with the same air flow rate and pressure. The bulk density of the powder was measured by the Scott volumetric method. The powder was placed into a sieve of the combined funnel on the upper part of the distribution box; the powder flew into the distribution box by vibration, and alternately passed through 4 glass plates with an inclination angle of 25° and the square funnel in the distribution box. After filling the container, the bulk density of the sample can be obtained according to the mass of the powder and the volume of the container. The measurement method of tap density was to weigh a certain mass of powder, put it into a measuring cylinder, and fix the measuring cylinder on a bracket so that it can move up and down; the vibration frequency was set to 250 times per minute, and the total time was 12 min. The tap density can be calculated by measuring the volume of the powder in the measuring cylinder.

Compared to the W-1 sample with micrometer-sized RE oxides, the W-2 sample with nanometer-sized RE oxides exhibits lower porosity, and its bulk density and tap density are greatly improved. The specific results are shown in Table 1. The uniformly mixed RE oxide-tungsten powder was subjected to cold isostatic pressing and then sintered in an intermediate frequency induction furnace. The heating rate of the fritting furnace was sequentially set as 280, 276, 276, 278, and 277 K·min^{-1}, until the sintering temperature reached 2623 K. The microstructure of the sintered sample is shown in Fig. 2. Combined with the EDS analysis (Table 2), the bright area in the view represents the W matrix, while the dark area is the second phase.

After multiple passes of swaging, drawing, and high-

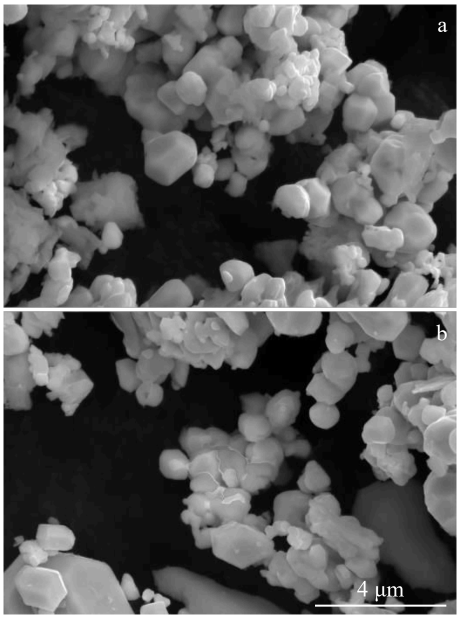

Fig.1 SEM morphologies of W-La_2O_3-Y_2O_3-ZrO_2 powder samples: (a) W-1 and (b) W-2

Table 1 Test results of raw materials

Sample	Powder mixing method	Porosity	Fisher particle size/μm	Bulk density/g·cm^{-3}	Tap density/g·cm^{-3}
W-1	Ball-milling	0.727	1.29	2.28	4.85
W-2	Ultrasonic-wave	0.645	1.62	3.33	6.67

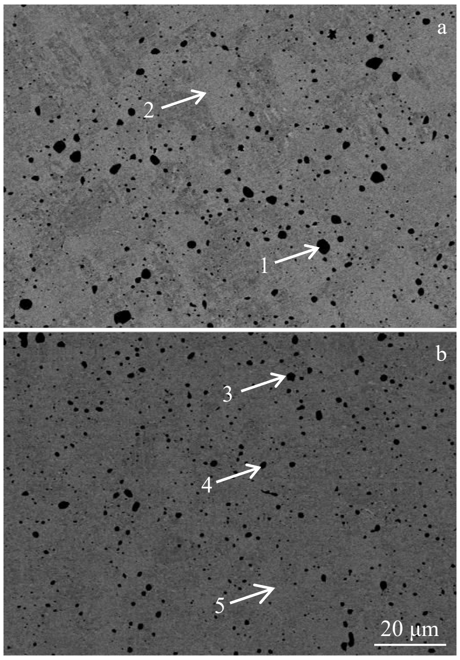

Fig.2 SEM images of sintered samples: (a) W-1 and (b) W-2

frequency annealing depending on the state of the sample during the process, a tungsten cathode with a diameter of 3 mm was finally prepared. The microstructure of the cathode sample is shown in Fig. 3. The second phase is distributed as thin strips in the machining direction, while some coarse features of the second phase still exist in it. The EDS analysis indicates that the coarse features belong to the La-Zr-O phase, while the thin strip-shaped second phase is mostly the La-O phase. The statistical analysis shows that the average size of the second phase of W-1 is 0.72 μm, while that of the W-2 sample is 0.46 μm, representing a decrease of nearly 36%, while the proportion of small-sized particles is significantly increased.

The cathode was sharpened and assembled into a welding torch. The welding device is shown in Fig.4. The TIG welding current was set to 250 A, the starting current was set to 90 A, and the working time was set to 0.5, 1, and 2 h. The YC-300WX welding machine was set to DC welding mode. During the TIG welding process, the measurement error of the temperature of the tungsten cathode's tip was extremely large due to the interference of arc plasma. Therefore, the COMSOL Multiphysics software was used to simulate the temperature distribution in different regions of the cathode tip.

Table 2 EDS results of point 1 – 5 marked in Fig. 2a and 2b (wt%)

Point	W	La	Y	Zr	O	C
1	-	82.56	3.66	5.74	8.04	-
2	96.49	-	-	-	-	3.51
3	4.86	71.49	4.42	3.23	16.00	-
4	8.90	76.40	3.52	2.24	8.93	-
5	96.37	-	-	-	0.61	3.02

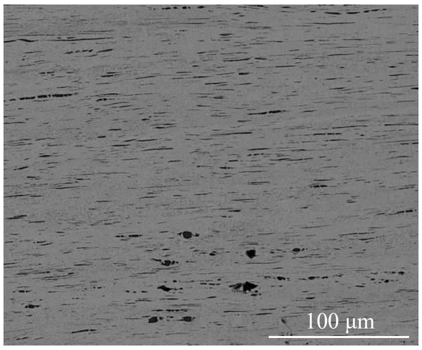

Fig.3 Microstructure of multi-pass machining of 3-mm diameter tungsten cathode

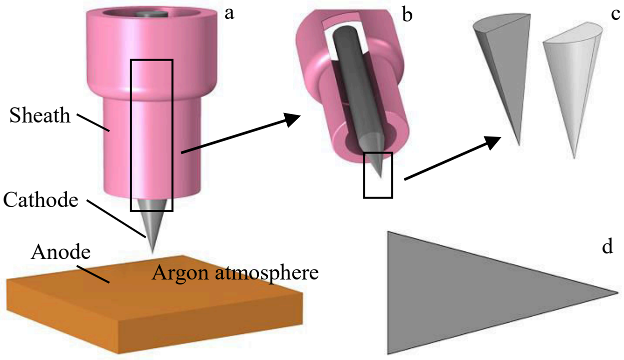

Fig.4 Schematic diagram of TIG device (a); detail view (b); preparation of the metallographic sample with the axial section of the tip (c); metallographic sample (d)

2 Results and Discussion

2.1 Cathode performance test

As the working temperature of the cathode increases, the cathode tip melts and deforms or even burns out. During the heat transfer from the tip to the cathode body, the burnout area gradually migrates from the cathode tip to the base and becomes larger. Fig.5 shows the macroscopic morphologies of the burning loss, showing that the tip of the W-1 sample is burned off while the W-2 sample exhibits higher stability with the same working time. The difference in the cathode quality before and after welding was measured by an electronic balance. The specific results are shown in Fig. 6. The burning quality of the W-2 sample is significantly lower than that of the W-1 sample, and the cathode burning loss at 2 h is decreased by nearly 85.4%. Fig. 7a – 7d show the metallographic structures of the sample after TIG welding. During high-temperature operation, different degrees of recrystallization and grain growth occur in the heated area of each sample, and black aggregated areas with different sizes appear inside the cathode, which are not seen in the original cathode. The EDS surface scan results of each element of the W-2 sample are shown in Fig. 7f. The black area contains a large amount of La and O.

After multi-pass processing in the early stage, various

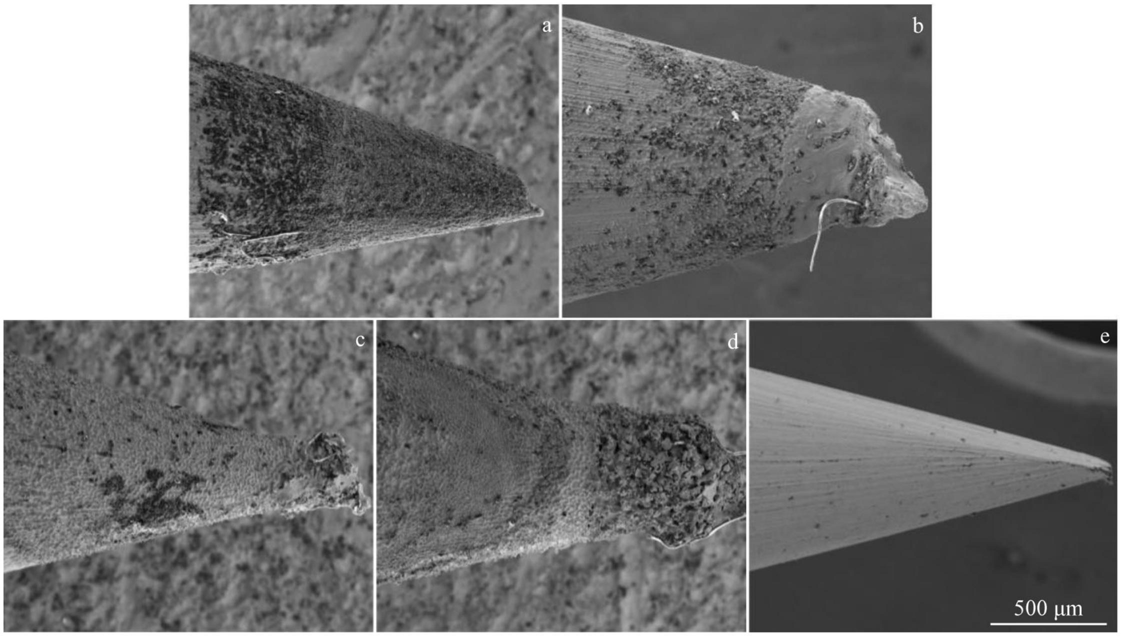

Fig.5 Burnout macromorphologies of the electrode tip with different welding time: (a) W-1, 1 h; (b) W-1, 2 h; (c) W-2, 1 h; (d) W-2, 2 h; (e) without welding

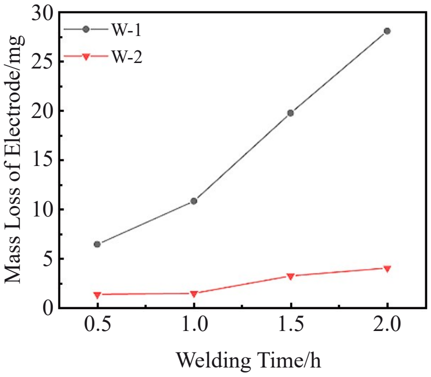

Fig.6 Mass loss comparison of the TIG-welded samples

defects and internal stress may form and gradually accumulate inside the material, making it thermodynamically unstable. During the TIG process with the prepared cathode, a high-frequency voltage spark induces discharge between the cathode and the base metal, causing space ionization and gradually increasing the loop current in the discharge range of the arc. In this process, the cathode collides with positive and negative ions to obtain energy so that the surface temperature of the electrode rises rapidly, and the temperature inside the electrode gradually increases. When atoms have sufficient mobility, they migrate to the equilibrium position with lower energy so that the internal stress can be relaxed and the stored energy is gradually released. If the area where evaporation and melting occur due to high temperatures is temporarily ignored, the effect of high temperatures gradually reduces or eliminates the deformation damage caused by the pre-processing of the inner area, so the working process of the electrode can be regarded as a kind of “annealing” treatment. With the release of the stored deformation energy, the matrix changes from a deformed state to a low-energy state and from an unstable state to a stable state.

Considering the metallographic structure, the sample can be roughly divided into three regions. According to its shape and distribution, the second phase in region C is strip-shaped or streamlined; region B is close to the working surface, where the second phase is spherical or quasi-spherical; in region A, which is the closest area to the arc center, the second phase is massively aggregated with an extremely irregular shape, and the migration along the grain boundary can be observed. Temperature gradients in different regions of the tip are important factors affecting the material's evolution. For the low degree of heating in region C, the grains are recovered from fibrous to flat, and still distributed along the machining direction. Due to the high temperature of region B and region A, different degrees of recrystallization and grain growth occur after recovery. To further analyze the evolution of the material, we need to understand the temperature distribution at the tip.

2.2 Simulation of temperature field in the welding area

2.2.1 Geometric model

According to the TIG device shown in Fig.4, copper is used as an anode, the RE-tungsten is used as a cathode, and the calculation model is composed of three parts: the cathode area, the argon area, and the anode area. Considering the overall structural symmetry in the experiment, the three-dimensional model is simplified to a two-dimensional axisymmetric model, as shown in Fig. 8. The calculation area is a rectangle with 20 mm×87.5 mm in dimension, the radius of the tungsten electrode is 1.5 mm, the cathode-anode separation is 3 mm, the tip taper angle is 30°, and the width of

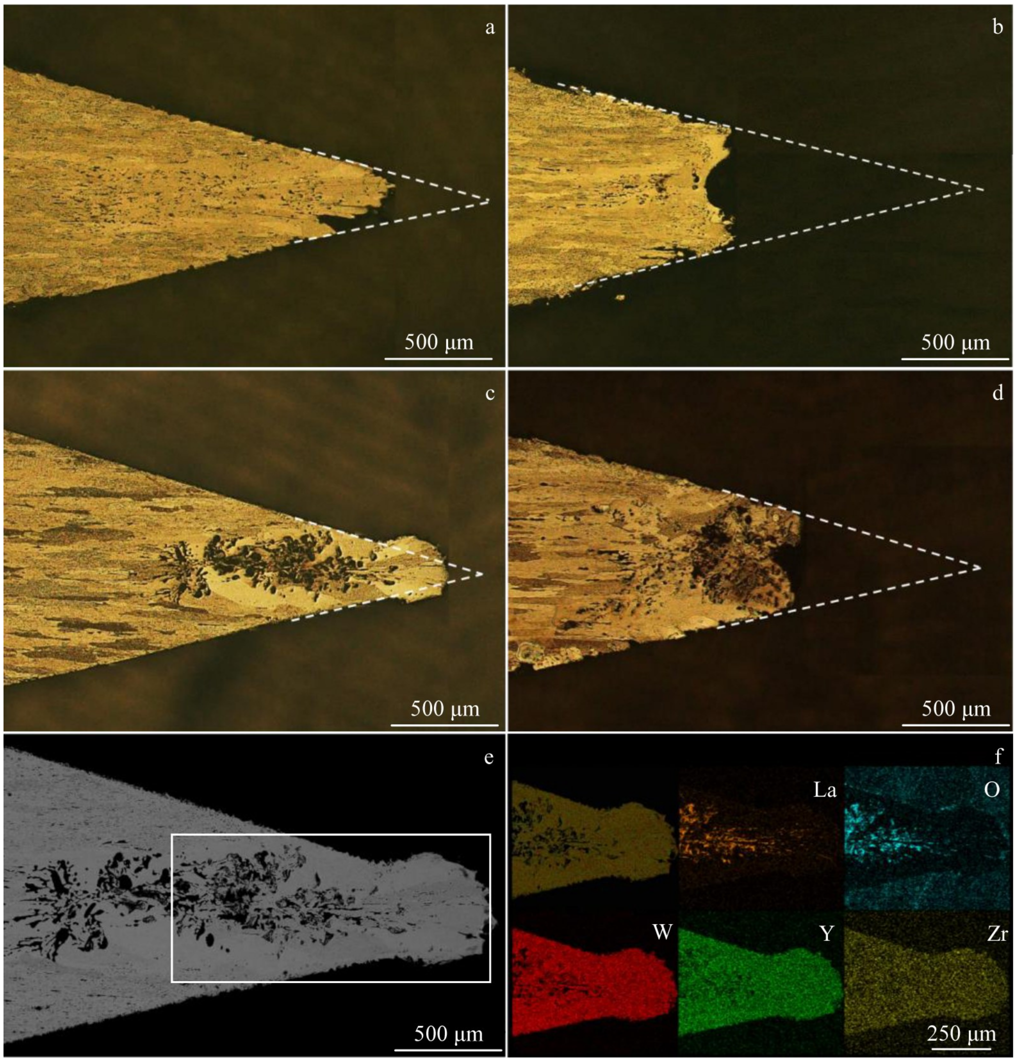

Fig.7 Metallographic structures of TIG-welded samples: (a) W-1, welding time 1 h; (b) W-1, welding time 2 h; (c) W-2, welding time 1 h; (d) W-2, welding time 2 h; (e) SEM image of the microstructure of the W-2 sample; (f) EDS mappings of the white square area for W-2 sample marked in Fig.7e

the argon gas inlet is 1.5 mm.

2.2.2 Coupling of physics

During the arcing process, the temperature inside the tungsten cathode depends on the Joule heat generated by the external direct current, the heat conduction inside the cathode, and the convective heat transfer between the arc and the electrode[33]. To facilitate the simulation of the temperature field inside the cathode, we assumed that the plasma is in local thermodynamic equilibrium[34–36], and that the plasma flow is laminar; the anode area does not include melting effects, and the anode shape is assumed to be fixed in space and time.

The differential equation governing the arc and the cathode is as follows.

Mass conservation equation:

$$\partial\rho/\partial t + \nabla\cdot(\rho\boldsymbol{u}) = 0 \tag{1}$$

Energy conservation equation:

$$\rho C_{\mathrm{p}}\frac{\partial T}{\partial t} + \rho C_{\mathrm{p}}\boldsymbol{u}\cdot\nabla T = \nabla\cdot(k\nabla T) + Q \tag{2}$$

$$Q = \frac{\partial}{\partial T}\left(\frac{5k_{\mathrm{B}}T}{2q}\right)(\nabla T\cdot\boldsymbol{J}) + \boldsymbol{E}\cdot\boldsymbol{J} + Q_{\mathrm{rad}} \tag{3}$$

Momentum conservation equation:

$$\rho\frac{\partial u}{\partial t} + \rho(\boldsymbol{u}\cdot\nabla)\boldsymbol{u} = \nabla\cdot(-\rho\boldsymbol{\iota} + \boldsymbol{\kappa}) + \boldsymbol{F} \tag{4}$$

$$\boldsymbol{\kappa} = \mu[\nabla\boldsymbol{u} + (\nabla\boldsymbol{u})^{T}] - \frac{2}{3}\mu(\nabla\boldsymbol{u})\boldsymbol{\iota} \tag{5}$$

$$\boldsymbol{F}=\boldsymbol{J}\times\boldsymbol{B} \tag{6}$$

Current-Magnetic field coupling equation:

$$\boldsymbol{J}_{\mathrm{mf(ec)}} = -\sigma(E_{\mathrm{ec}}+E_{\mathrm{mf}}) \tag{7}$$

$$\boldsymbol{E}_{\mathrm{mf}} = -\frac{\partial\boldsymbol{A}}{\partial t} \tag{8}$$

$$\boldsymbol{E}_{\mathrm{ec}} = -\nabla V \tag{9}$$

$$\boldsymbol{B} = \nabla\times\boldsymbol{A} \tag{10}$$

These equations describe the physical conditions of the arc and the cathode, where ρ is the density, t is the time, $\boldsymbol{u}$ is the velocity vector, C_{p} is the isobaric heat capacity, T is the absolute temperature, k is the thermal conductivity, Q is the heat source, k_B is the Boltzmann constant, q is the electron charge, $\boldsymbol{J}$ is the current density vector, $\boldsymbol{E}$ is the electric field strength vector, Q_{rad} is the total volume radiation coefficient, $\boldsymbol{\iota}$ is the unit matrix vector, μ is the dynamic viscosity, F is the Lorentz force, and B is the magnetic flux density vector of the self-induced magnetic field. In the subscript of $\boldsymbol{J}_{mf(ec)}$, mf represents the magnetic field and ec represents the electric field. σ is the electrical conductivity, $\boldsymbol{A}$ is the magnetic vector potential, and V is the electric potential. Each vector item includes its r-component, phi-component, and z-component.

2.2.3 Boundary conditions

The experimental parameters required for the input of the model include the electrode size, external welding current (A), the flow rate of protective argon gas ($m \cdot s^{-1}$), and temperature (K) of circulating cooling water inside the welding torch. The temperature field distribution of the tungsten cathode is obtained by coupling multi-physics fields, such as electric field, magnetic field, fluid heat transfer, and laminar flow field in COMSOL.

In the geometric model shown in Fig. 8, the physical parameters of the material are all from the COMSOL material library. For setting the boundary conditions of the electric field, the *fghi* boundary is set to electrical insulation; the *def* boundary is set to ground; the external welding current is 250 A DC, placed along the *ia* boundary in the way of current density in the model. In the flow field boundary conditions, the *fgh* boundary is set as an open boundary; argon is fed from the *hi* boundary at a flow rate of 6.27 m s^{-1}. In the heat transfer module, the initial value of the temperature is set to 300 K; to facilitate the convergence of the calculation, the temperature of the *fghi* boundary is set to be constant at 300 K during the calculation; the temperature of the circulating cooling water is 288 K, so the *ij* boundary temperature in the model is set to 288 K.

2.2.4 Simulation results

Fig. 9 shows the calculated results under a welding current of 250 A. The maximum temperature of the arc reaches 19 000 K, which is lower than the calculated results reported in Ref.[37–38], plausibly due to the difference for the content and species of doped REs and different model settings for the cathode sheath area.

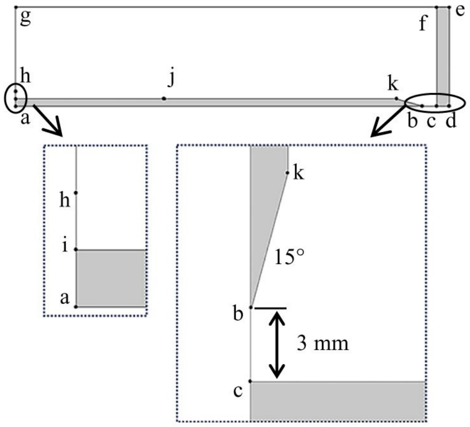

Fig.8 Geometric model of TIG welding device

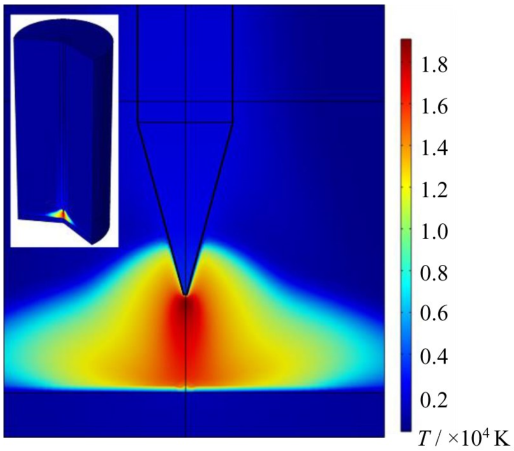

Fig.9 Calculation results of TIG welding temperature field

In the calculation process, the cathode and the arc temperature rapidly increase within 400−600 ms after the arc ignition and reach the temperature peak, after which the temperature remains almost constant during the welding process. During the arcing process, the RE elements migrate and diffuse to the surface of the tip, and the amount of migrated RE elements at different positions of the tip are different, which leads to differences in the RE active layer on the surface of the tip, further causing regional differences in surface work function and affecting the electron emission properties of the cathode. High external energy is required to maintain the stable arc combustion when the electron emission capacity is low, so there may be abnormally high or low temperatures in this area. Therefore, during the working process for the same cathode, the temperature of the tip surface does not exhibit a uniform and smooth transition. In actual cases, the temperature of a certain area on the tip surface may suddenly increase, affecting the heat transfer field inside the cathode.

To further revise the model and to approach the real behavior, the factors of the surface work function change are added to the model, referring to Ref. [39] and previous experimental results of our research group. According to the burnout state reflected by the metallographic structure, a numerical function of the effective work function is attached along the conical surface. The highest value of 4.6 eV is at the tip, calculated for pure tungsten, and the lowest value of 3.37 eV is calculated using the test result of the RE-tungsten cathode with the same specification from our previous research, which is set at a position with strong RE aggregation. The rest of the function points are smoothed, and the iterative result is shown in Fig.10.

Masao et al[40] found in their experiments that the temperature of the W-La_2O_3 cathode tip changes little with the arc working time. Herein, the temperature is almost constant, fluctuating no more than 100 K, the temperature of the entire cone tip is distributed in the range of 3000 – 3500 K as a

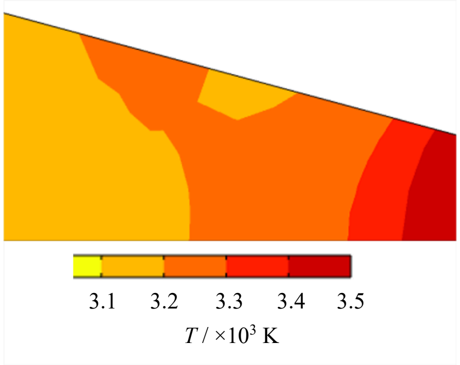

Fig.10 Simulation results of local temperature field at the cathode tip

whole[34], and the overall temperature distribution range is not large. Therefore, the output image at the temperature equivalent interval of 100 K is selected as the calculation result in this research. The corresponding average temperatures of regions A, B, and C are 3350, 3250, and 3150 K, respectively.

2.3 Calculation of diffusion activation energy Q of the second phase

During the welding process, affected by numerous external factors, the welding head fuses to varying degrees, and we cannot get the blown part. Therefore, when calculating the cross-sectional area of the second phase, according to the tip morphology and the metallographic structure of the sample after welding, we selected the area at a certain distance from the tip, showing three particular regions for analysis. Fig.11a–11f show the cathode tips (region A, with an axial distance of 1200 – 1500 μm from the original tip), the flanks of the tip (region B, with an axial distance of 1000–2000 μm from the original tip), and interior (region C, with an axial distance of 1200–2000 μm from the original tip). The calculation results of equivalent diameters converted from the average area are listed in Table 3. During the high-temperature operation process, the average equivalent size of the second phase in region C of the two samples is about 0.3 μm. After working for 1 h, the second phase in region B of both samples reaches a size of about 1 μm. When the welding time is 2 h, the equivalent average size of the second phase of W-1 and W-2 reaches 1.12 and 1.38 μm, respectively. In region A, the W-1 and W-2 samples show two distinct states. With the working time up to 2 h, the average equivalent size of the second phase in the W-1 sample is 2.11 μm. The W-2 sample reaches 4.10 μm after 0.5 h of operation, while it is 10.86 μm after 2 h. The second-phase particles almost completely occupy the grain boundaries and are distributed in a dendritic shape, as shown in Fig.7.

During the welding process, the evaporation and consumption of RE elements in the high-temperature area decrease their concentration on the surface, resulting in many crystal defects, such as vacancies, and enhancing the diffusion driving force of RE elements. At the same time, the loss of RE elements at the grain boundary enlarges the grain boundary area and increases the grain boundary energy. Under the combined action of these factors, a high concentration gradient is formed between the surface and the interior, and the RE elements diffuse from the interior to the surface. However, it

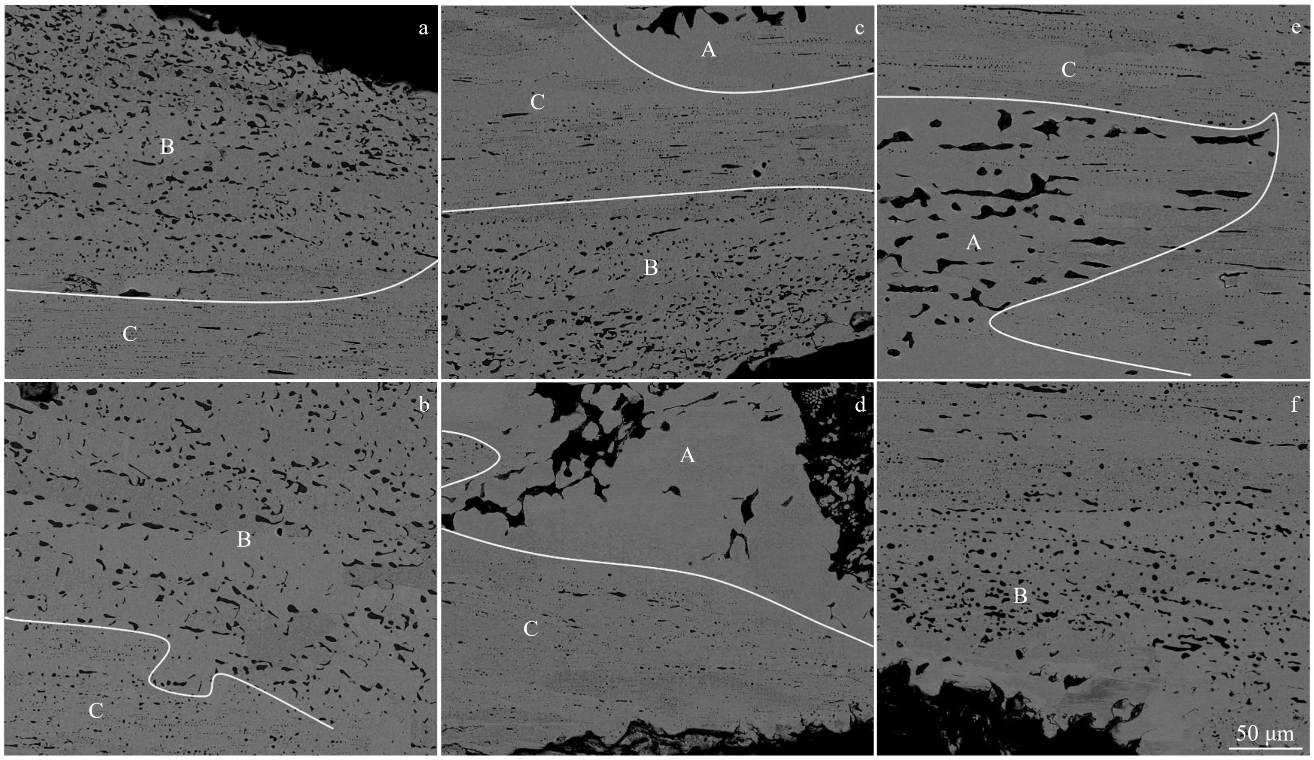

Fig.11 SEM images and schematic diagram of microstructure of the cathode tip: (a–d) W-2 and (e–f) W-1

Table 3 Calculation results of equivalent size of the second phase in W-1 and W-2 samples

Welding time/h	Equivalent size of W-1/μm			Equivalent size of W-2/μm		
	Region A	Region B	Region C	Region A	Region B	Region C
0	0.320 295	0.331 894	0.322 923	0.310 463	0.302 122	0.315 468
0.5	0.352 529	0.342 841	0.323 291	4.109 051	0.567 767	0.289 106
1	1.910 107	1.047 857	0.344 485	5.654 024	0.944 282	0.317 265
2	2.115 835	1.124 181	0.353 517	10.859 804	1.381 681	0.354 714

requires a certain energy barrier, which is generally referred to as diffusion energy, Q, and only those atoms with energy higher than the diffusion energy can migrate and diffuse to the cathode surface. It is known that the kinetic energy of atoms follows the Maxwell-Boltzmann distribution, and that temperature greatly influences the diffusion of metal atoms, the migration and growth of the second phase, and the migration of grain boundaries, so the diffusion rate of active substances should be proportional to $\exp(-Q/kT)$ [41]. In addition, the diffusion rate is positively correlated to the size change of the second phase. Combined with Beck's formula[42], the following equation can be obtained:

$$D_t-D_0=t^nK \quad (11)$$

$$K=A\exp(-Q/kT) \quad (12)$$

where t is the working time, D_t is the equivalent diameter of the second phase at t, n is the sensitivity coefficient, A is a constant related to the temperature and the concentration of active substances in the material, and k is the Boltzmann constant. Taking the logarithm on both sides of Eq.(11), we obtain the following equation:

$$\ln(D_t-D_0)=n\ln t+\ln K \quad (13)$$

It can be found that $\ln(D_t-D_0)$ is proportional to $\ln t$, so Eq.(13) can be regarded as an oblique intercept straight line equation, and the intercept obtained by fitting the straight line is the coefficient $\ln K$ related to the required diffusion energy Q. Substitute the data in Table 3 into the formula, the fitting results are shown in Fig.12 and Fig.13, and Table 4 lists the calculated data.

Taking the logarithm for Eq.(12), we can get the equation:

$$\ln K=-Q/kT+\ln A \quad (14)$$

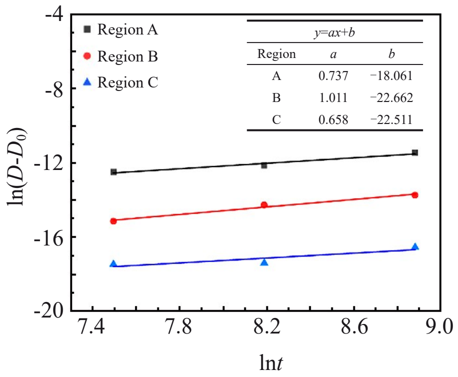

$y=ax+b$		
Region	a	b
A	0.737	−18.061
B	1.011	−22.662
C	0.658	−22.511

Fig.13 $\ln(D-D_0)$ -$\ln t$ curves of W-2

Table 4 Values of lnK after fitting in different regions

Region	W-1	W-2
A	−38.357	−18.060
B	−40.802	−22.662
C	−45.004	−22.511

Likewise, $\ln K$ is proportional to $(-1/T)$. Combined with the temperature of each region obtained from the COMSOL-simulated temperature field, the results of data fitting are shown in Fig.14. The slope of the straight line is positively correlated to the diffusion energy Q of the corresponding material. The calculation shows that the diffusion activation energy Q of the second phase is decreased by nearly 34% in W-2 compared with W-1, indicating that the RE elements in W-2 are more likely to diffuse to the cathode surface, which is consistent with the experimental phenomenon. In region C, with the welding time reaching 2 h, the average size of the second phase in both W-1 and W-2 samples is increased by 12.9%; in region B, the growth amount reaches 261.3% and

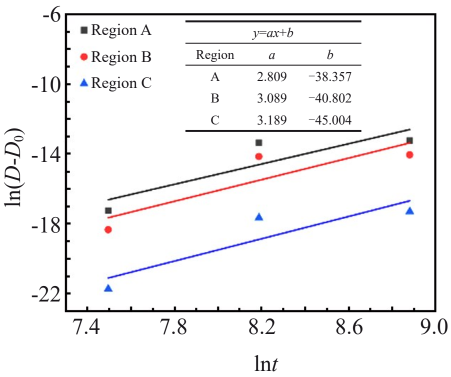

$y=ax+b$		
Region	a	b
A	2.809	−38.357
B	3.089	−40.802
C	3.189	−45.004

Fig.12 $\ln(D-D_0)$ -$\ln t$ curves of W-1

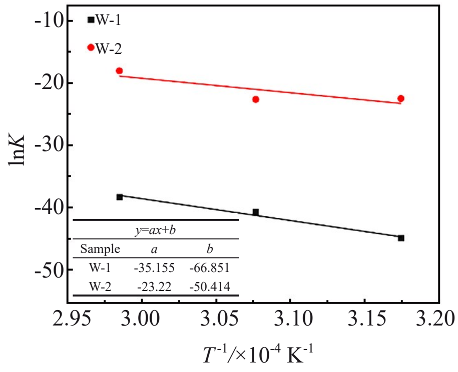

$y=ax+b$		
Sample	a	b
W-1	-35.155	-66.851
W-2	-23.22	-50.414

Fig.14 $\ln K$-T^1 curves of W-1 and W-2 samples (W-1)

345.2% for W-1 and W-2 samples, respectively. The above two regions exhibit no obvious difference from the statistical results, but in region A, the second phase of the W-2 sample is increased by nearly 1200% after 0.5 h of operation, and 3400% after 2 h of operation. The growth of the W-1 sample is only 12.9% and 580.6% after 0.5 and 2 h of operation, respectively.

The stable balance between the diffusion mobility of RE to the cathode surface and the evaporation rate is the key to maintain the high electron emission capacity of the cathode, and grain boundaries are the main channels for diffusion and migration. In region C and or the area farther from the tip, the average equivalent size of the second phase remains approximately 0.3 μm, and the effective pinning action keeps the recovery and recrystallization degree of the matrix structure at a low level, enabling the subsequent migration and diffusion of RE elements. In the A and B regions, the high temperature provides energy for the material evolution. On the one hand, the dispersed second phase increases the total interfacial energy inside the system. To alleviate this unstable state, the second phase tends to coarsen so that large particles grow while small particles dissolve[43]; on the other hand, the concentration gradient inside and outside the material allows the internal RE elements to migrate to the surface, and these two aspects simultaneously act, causing the coarsening of the second phase.

Region A is the frontier of electron emission, and the difference in the morphology of RE oxides in this region significantly affects the material's performance. As mentioned above, the tip grains of the W-1 sample grow sharply due to the absence and uneven distribution of the second phase, as shown in the white boxed area in Fig. 15. Otherwise, because of the lack of RE, the grains have no time to grow, and electron emission is preferentially carried out at the grain boundaries containing high energy, and cracking occurs directly along the grain boundaries, as shown in Fig.7a.

From Fig. 7c and 7d, a large amount of the second phase aggregates can be found at the tip of the W-2 sample, opposite to the tip of the W-1 sample in Fig.7a and 7b. Like the Zener pinning mechanism of the grain boundaries by the dispersed second-phase particles, this dendritic-like second-phase in region A of the W-2 sample seems to play a role in hindering the grain growth. And the strip-shaped grains retain part of the grain boundaries, ensuring the diffusion channel of RE elements. Under the same working conditions, its internal structure has higher stability, making the burning loss quality of the W-2 sample significantly lower than that of the W-1 sample, which is consistent with the experimental results.

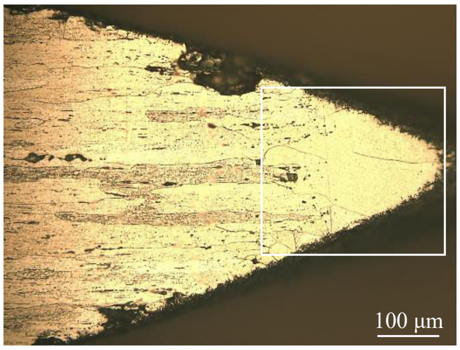

Fig.15 Extra-large grains at the tip of the cathode of W-1

3 Conclusions

1) W-1.5La_2O_3-0.1Y_2O_3-0.1ZrO_2 cathode samples were prepared with nanometer- and micrometer-sized rare-earth (RE) oxides (La_2O_3, Y_2O_3) and tungsten powder as starting materials. TIG welding was performed on the samples under the same current. During electron emission, the second phase gradually changes its morphology from the initial diffusing appearance to a concentrated area at the emission tip. The variations in size and morphology affect the evolution of different regions (A, B, C) of the material.

2) The second phase at the tip of the sample doped with micrometer-sized RE oxides is rapidly consumed, while the internal active substances cannot be replenished in time, so the secondary recrystallization of the structure is caused, and the reduction of grain boundary worsens the diffusion ability of RE elements.

3) In the sample doped with nanometer-sized RE oxides, the second phase at the tip almost completely occupies the grain boundary position, exhibiting an extremely irregular dendritic morphology, which effectively curbs the appearance of coarse grains while retains a large number of grain boundaries. It creates favorable conditions for the diffusion of RE elements.

4) Combined with the simulated temperature field, it is found that the diffusion activation energy of the second phase is decreased by nearly 34% during the welding process, which improves the electron emission performance of the cathode. As a result, the cathode burn-off is decreased by nearly 85.4%.

References

1 Kim Youngmoo, Hong Moon-Hee, Lee Sung Ho *et al. Metals and Materials International*[J], 2006, 12(3): 245

2 Mabuchi M, Okamoto K, Saito N *et al. Materials Science & Engineering A*[J], 1997, 237(2): 241

3 Daoush W M R, Elsayed A H A, Kady O A G E *et al. Metallurgical and Materials Transactions A*[J], 2016, 47: 2387

4 Chen Y, Wu Y C, Yu F W *et al. International Journal of Refractory Metals and Hard Materials*[J], 2007, 26(6): 525

5 Chen Y, Wu Y C, Yu F W *et al. Rare Metal Materials and Engineering*[J], 2007, 36(5): 822 (in Chinese)

6 Lang E, Schamis H, Madden N *et al. Journal of Nuclear Materials*[J], 2021, 545: 152 613

7 Yang X B, Tang H P, Zhu J L *et al. Rare Metal Materials and Engineering*[J], 2022, 51(8): 3025

8 Guo X C, Liu Z J, Li H B *et al. Rare Metal Materials and Engineering*[J], 2021, 50(3): 902

9 Zheng X, Bai R, Wang D H *et al. Rare Metal Materials and*

Engineering[J], 2011, 40(10): 1871 (in Chinese)

10 Yang Z M, Wang W, Ogawa Yoji *et al. Rare Metal Materials and Engineering*[J], 2005, 34(11): 1806 (in Chinese)

11 Wang J F, Zuo D W, Zhu L *et al. International Journal of Refractory Metals and Hard Materials*[J], 2018, 71: 167

12 Zhao M Y, Zhou Z J, Ding Q M *et al. International Journal of Refractory Metals and Hard Materials*[J], 2015, 48: 19

13 Zong X, Lu Y X. *Mining & Processing Equipment*[J], 2010, 38(22): 1

14 Du Y B, Liu Z G, Cui S. *Chinese Journal of Rare Metals*[J], 2011, 35(3): 378 (in Chinese)

15 Raabe Dierk. *Physical Metallurgy*[M]. Amsterdam: Elsevier, 2014: 2291

16 Zan X, Gu M, Wang K *et al. Fusion Engineering and Design*[J], 2019, 144: 1

17 Wang F Z, Zhang H, Ding B J *et al. Materials Science & Engineering A*[J], 2002, 336(1): 59

18 Guo X C, Liu Z J, Li H B *et al. Rare Metal Materials and Engineering*[J], 2022, 51(5): 1879

19 Zhang H, Yang Z M, Ding B J *et al. IEEE Transactions on Components and Packaging Technologies*[J], 1999, 22(3): 455

20 Zhang H, Chen X F, Yang Z M *et al. Materials Letters*[J], 1999, 38(6): 401

21 Zhuge F, Ye Z Z, Wang F Z *et al. Materials Letters*[J], 2003, 57(19): 2776

22 Zheng H J, Huang J G, Wang W *et al. Electrochemistry Communications*[J], 2005, 7(10): 1045

23 Wang F Z, Zhuge F, Zhang H *et al. Materials Research Bulletin*[J], 2003, 38(4): 629

24 Hussein Gamal A M, Ismail Hamdy M. *Colloids and Surfaces A: Physicochemical and Engineering Aspects*[J], 1995, 99(2):129

25 Kim Youngmoo, Lee Kyong Ho, Kim Eun-Pyo *et al. International Journal of Refractory Metals and Hard Materials*[J], 2009, 27(5): 842

26 Wang L Y, Yu Y G, Peng Y *et al. Nonferrous Metals Engineering*[J], 2019, 9(10): 21

27 Liu R, Zhou Y, Hao T *et al. Journal of Nuclear Materials*[J], 2012, 424(1–3): 171

28 Liu T, Fan J L, Huang B Y *et al. Rare Metal Materials and Engineering*[J], 2010, 39(2): 314 (in Chinese)

29 Veleva L, Schaeublin R, Battabyal M *et al. International Journal of Refractory Metals and Hard Materials*[J], 2015, 50: 210

30 Eric Lang, Nathan Madden, Charles Smith *et al. International Journal of Refractory Metals and Hard Materials*[J], 2018, 75: 279

31 Makoto Fukuda, Akira Hasegawa, Shuhei Nogami *et al. Journal of Nuclear Materials*[J], 2014, 449: 213

32 Xie Z M, Zhang T, Liu R *et al. International Journal of Refractory Metals and Hard Materials*[J], 2015, 51: 180

33 Jnsson P G, Szekely J, Choo R T C *et al. Modelling and Simulation in Materials Science and Engineering*[J], 1994, 2 (5): 995

34 Lowke JJ, Morrow R, Haidar J. *Journal of Physics D: Applied Physics*[J], 1997, 30(14): 2033

35 Lu F G, Yao S, Lou S N *et al. Computational Materials Science*[J], 2004, 29(3): 371

36 Massoud Goodarzi, Roland Choo, James M Toguri. *Journal of Physics D: Applied Physics*[J], 1997, 30: 2744

37 Haidar J. *Journal of Applied Physics*[J], 1998, 84(7): 3518

38 Zhu P Y, Lowke JJ, Morrow R. *Journal of Physics D: Applied Physics*[J], 1992, 25(8): 1221

39 Cram L E. *Journal of Physics D: Applied Physics*[J], 1983, 16(9): 1643

40 Masao Ushio, Alber A Sadek, Fukuhisa Matsuda. *Plasma Chemistry and Plasma Processing*[J], 1991, 11(1): 81

41 Wang H T, Fang Z Zak, Hwang Kyu Sup. *Metallurgical and Materials Transactions A*[J], 2011, 42(11): 3534

42 Burke J E, Turnbull D. *Progress in Metal Physics*[J], 1952, 3: 220

43 Du Z Y, Lv Y Q, Han Y *et al. Tungsten*[J], 2021, 2(4): 371

纳米级和微米级稀土氧化物掺杂W-La_2O_3-Y_2O_3-ZrO_2阴极尖端的组织和性能

郭胤宸[1]，杨建参[1]，周绍欣[1]，袁德林[2]，聂祚仁[1]

(1. 北京工业大学 材料科学与工程学院，北京 100124)

(2. 江西应用技术职业学院，江西 赣州 341000)

摘　要：使用粉末冶金法将纳米级（70–80 nm）和微米级（500–600 nm）稀土氧化物（La_2O_3，Y_2O_3）与钨粉混合，随后通过冷等静压、中频感应烧结、旋锻、拉拔等一系列工艺制备了W-1.5La_2O_3-0.1Y_2O_3-0.1ZrO_2（质量分数，%）材料。对含有纳米和微米尺寸稀土氧化物的阴极样品使用相同的焊接电流，分别进行了0.5、1、2 h的氩弧焊。结果表明，具有纳米级稀土氧化物的样品在焊接过程中表现出更高的工作稳定性，烧损同比降低了近85.4%。此外，随着工作时间的延长，阴极尖端不同区域的稀土氧化物聚集度显著增加。结合COMSOL Multiphysics温度模拟发现，第二相的扩散活化能降低了近34%。这是因为更为细小的第二相有效地控制了钨基体组织的演变，保留了大量晶界作为通道，促进了活性物质在电子发射过程中的扩散。

关键词：W-La_2O_3-Y_2O_3-ZrO_2；钨阴极；氩弧焊；稀土氧化物；纳米级；微米级；COMSOL Multiphysics

---

作者简介：郭胤宸，男，1997年生，硕士，北京工业大学材料科学与工程学院，北京 100124，E-mail：cyg8786@163.com